Power Electronic Systems
Laboratory



IEEE Transactions on Industry Applications, Vol. 51, No. 1, pp. 509-520, January/February 2015

# Weight Optimization of a Cooling System Composed of Fan and Extruded-Fin Heat Sink

C. Gammeter,
F. Krismer,
J. W. Kolar



Eidgenössische Technische Hochschule Zürich
Swiss Federal Institute of Technology Zurich

# Weight Optimization of a Cooling System Composed of Fan and Extruded-Fin Heat Sink

Christoph Gammeter, *Student Member, IEEE*, Florian Krismer, *Member, IEEE*, and Johann W. Kolar, *Fellow, IEEE*

***Abstract*—This paper details the weight optimization of forced convection cooling systems, composed of a fan and an extruded-fin heat sink, required for a dc–dc converter of an airborne wind turbine system. The presented investigations detail the optimization of the heat sink's fins with respect to minimum weight and the selection of a suitable fan for minimum overall system weight. A new analytical cooling system model is introduced, and the calculated results are compared to the results determined with a preexisting analytical model and finite-element model simulations. The comparison to experimental results demonstrates the accuracy improvements achieved with the proposed methods. Compared to commercially available products, a weight reduction of 52% is achieved with the proposed optimization procedure for the required heat sink system with $R_{\mathrm{th,S\text{-}a}} = 1$ K/W.**

***Index Terms*—Analytical models, electronics cooling, Pareto optimization, thermal analysis, thermal engineering, thermal management, thermal management of electronics, thermal resistance.**

## Abbreviations

| | |
|---|---|
| AWT | Airborne wind turbine. |
| DAB | Dual active bridge. |
| FB | Full bridge. |
| FEM | Finite-element modeling. |
| LV | Low voltage. |
| MV | Medium voltage. |
| NPC | Neutral point clamped. |
| UWT | Uniform wall temperature. |
| UWF | Uniform wall flux. |

## Greek Symbols

| | |
|---|---|
| $\gamma$ | Shape parameter for rectangular ducts $-0.3$ [$\mathbb{R}$]. |
| $\Delta p_{\mathrm{acc}}(\dot{V})$ | Conservation of momentum pressure drop characteristic of cooling system [Pa]. |
| $\Delta p_{\mathrm{duct}}(\dot{V})$ | Friction pressure drop characteristic of duct [Pa]. |
| $\Delta p_{\mathrm{fan}}(\dot{V})$ | Pressure drop characteristic provided in the fan data sheet [Pa]. |
| $\Delta p_{\mathrm{hs}}(\dot{V})$ | Friction pressure drop characteristic of heat sink [Pa]. |
| $\Delta p_{\mathrm{tot}}(\dot{V})$ | Total cooling system pressure drop characteristic [Pa]. |
| $\epsilon$ | Heat sink channel aspect ratio [$\mathbb{R}$]. |
| $\epsilon_{\mathrm{duct}}$ | Air duct aspect ratio [$\mathbb{R}$]. |
| $\eta$ | Fin efficiency [0, 1]. |
| $\lambda_{\mathrm{hs}}$ | Thermal conductivity of heat sink 210 [W/(m · K)]. |
| $\lambda_{\mathrm{air}}$ | Thermal conductivity of air 0.03 [W/(m · K)]. |
| $\nu_{\mathrm{air}}$ | Kinematic viscosity of the air $2.1\mathrm{E}^{-5}$ [$\mathrm{m}^2/\mathrm{s}$]. |
| $\rho_{\mathrm{air}}$ | Density of air 1.00 [$\mathrm{kg/m}^3$]. |
| $\sigma_{\Delta p_{\mathrm{tot}}}$ | Mean deviation of pressure drop [$\mathbb{R}$]. |

## Nomenclature

| | |
|---|---|
| $A_{\mathrm{eff}}$ | Effective convective surface area [$\mathrm{m}^2$]. |
| $A_{\mathrm{hs}}$ | Heat sink base plate area [$\mathrm{m}^2$]. |
| $c$ | Fin height [m]. |
| $c_{\mathrm{air}}$ | Thermal capacitance of air $1.01\mathrm{E}^3$ [J/(kg · K)]. |
| $C_1$ | Coefficient for UWT boundary conditions 3.24 [$\mathbb{R}$]. |
| $C_2$ | Coefficient for average Nusselt number 1.5 [$\mathbb{R}$]. |
| $C_3$ | Coefficient for UWT boundary conditions 0.409 [$\mathbb{R}$]. |
| $C_4$ | Coefficient for average Nusselt number 2 [$\mathbb{R}$]. |
| $d$ | Base plate thickness [m]. |
| $d_h$ | Hydraulic diameter of the heat sink channel [m]. |
| $D_h$ | Equivalent hydraulic diameter of heat sink channel and fin [m]. |
| $\overline{d}_{h,\mathrm{duct}}$ | Mean hydraulic diameter of duct [m]. |
| $f_{\mathrm{app}}(\dot{V})$ | Apparent friction factor of heat sink channel [$\mathbb{R}$]. |
| $f_{\mathrm{app,duct}}(\dot{V})$ | Apparent friction factor of duct [$\mathbb{R}$]. |
| $f\mathrm{Re}_{\sqrt{A}}$ | Friction factor Reynolds product [$\mathbb{R}$]. |
| $f\mathrm{Re}_{\sqrt{A},\mathrm{fd}}$ | Friction factor Reynolds product of fully developed flow [$\mathbb{R}$]. |
| $h$ | Average heat transfer coefficient [W/($\mathrm{m}^2$ · K)]. |
| $K_{\mathrm{sc}}$ | Sudden contraction friction factor [$\mathbb{R}$]. |
| $K_{\mathrm{se}}$ | Sudden expansion friction factor [$\mathbb{R}$]. |
| $K_{\mathrm{venturi}}$ | Venturi contraction friction factor (for $40^\circ \approx 0.2$) [$\mathbb{R}$]. |
| $L$ | Heat sink length [m]. |
| $L_{\mathrm{duct}}$ | Length of air duct [m]. |
| $L_{\mathrm{fan}}$ | Depth of fan [m]. |
| $L_h$ | Fluid dynamic entry length [m]. |

Manuscript received October 20, 2013; revised April 18, 2014; accepted June 27, 2014. Date of publication July 8, 2014; date of current version January 16, 2015. Paper 2013-IPPC-806.R1, presented at the 2013 IEEE Energy Conversion Congress and Exposition, Denver, CO, USA, September 16–20, and approved for publication in the IEEE TRANSACTIONS ON INDUSTRY APPLICATIONS by the Industrial Power Converter Committee of the IEEE Industry Applications Society.

The authors are with the Power Electronic Systems Laboratory, Swiss Federal Institute of Technology (ETH) Zürich, 8092 Zürich, Switzerland (e-mail: gammeter@lem.ee.ethz.ch; krismer@lem.ee.ethz.ch; kolar@lem.ee.ethz.ch).

Color versions of one or more of the figures in this paper are available online at http://ieeexplore.ieee.org.

Digital Object Identifier 10.1109/TIA.2014.2336977

| | |
|---|---|
| $L_h^+$ | Dimensionless fluid dynamic entry length [$\mathbb{R}$]. |
| $m$ | Model blending parameter [$\mathbb{R}$]. |
| $m_{\mathrm{cs}}$ | Total cooling system weight (fan, air duct, heat sink, and bottom plate) [kg]. |
| $n$ | Number of heat sink channels [$\mathbb{Z}$]. |
| $\mathrm{Nu}_{\sqrt{A}}$ | Nusselt number [$\mathbb{R}$]. |
| Pr | Prandtl number (air $\approx 0.71$) [$\mathbb{R}$]. |
| $\dot{V}$ | Volume flow through the heat sink [$\mathrm{m}^3/\mathrm{s}$]. |
| $R_{\mathrm{th,a}}$ | Thermal resistance of base plate to air [K/W]. |
| $R_{\mathrm{th,A}}$ | Thermal resistance of fin to air [K/W]. |
| $R_{\mathrm{th,conv}}$ | Equivalent convective thermal resistance [K/W]. |
| $R_{\mathrm{th},d}$ | Thermal resistance of base plate [K/W]. |
| $R_{\mathrm{th,fin}}$ | Thermal resistance of fin [K/W]. |
| $R_{\mathrm{th,S\text{-}a}}$ | Thermal resistance of cooling system [K/W]. |
| $R_{\mathrm{th,S\text{-}a,max}}$ | Maximum allowed thermal resistance of cooling system [K/W]. |
| $\mathrm{Re}_{\sqrt{A}}$ | Reynolds number [$\mathbb{R}$]. |
| $s$ | Heat sink fin spacing [m]. |
| $t$ | Heat sink fin thickness [m]. |
| $T_{\mathrm{amb}}$ | Ambient temperature [°C]. |
| $T_{\mathrm{amb,max}}$ | Maximum ambient temperature [°C]. |
| $T_{\mathrm{channel}}$ | Temperature in the heat sink channel [°C]. |
| $T_{\mathrm{hs,max}}$ | Maximum heat sink base surface plate temperature [°C]. |
| $T_{\mathrm{hs,min}}$ | Minimum heat sink base surface plate temperature [°C]. |
| $\overline{U}_{\mathrm{duct}}(\dot{V})$ | Mean fluid velocity in duct [m/s]. |
| $\overline{U}_{\mathrm{hs}}(\dot{V})$ | Mean fluid velocity in heat sink channel [m/s]. |
| $P_{\mathrm{loss}}$ | Dissipated losses [W]. |
| $P_{\mathrm{loss,max}}$ | Maximum dissipated losses [W]. |
| $z^\star$ | Dimensionless position of thermally developing flows [$\mathbb{R}$]. |

## I. Introduction

INCREASING consumption of electric energy, environmental issues, and limited availability of fossil fuels have led to a multitude of developments related to the generation of electricity from renewable energy sources. One innovative system in this context is the AWT detailed in [1], which generates electricity from high-altitude winds. High-altitude winds are known to be more stable and faster than winds close to the ground level and, thus, enable a more reliable and effective generation of electric energy [1].

The AWT is essentially a flying wing with a significantly lower construction effort of the power generation system compared to a traditional wind turbine. A long fiber and cable combination (tether $\approx 1$ km long) ties the AWT to the ground and, additionally, provides the electrical link to the ground station [1].

The greatest challenge with respect to the realization of the electric system of the AWT is to achieve a lightweight tether and lightweight generators and power converters. The considered AWT system is rated for a maximum input power of 100 kW, and related investigations detailed in [1] reveal that a low-weight realization of this AWT makes a dc–dc converter necessary, which boosts the dc bus voltage $V_1$ onboard the AWT

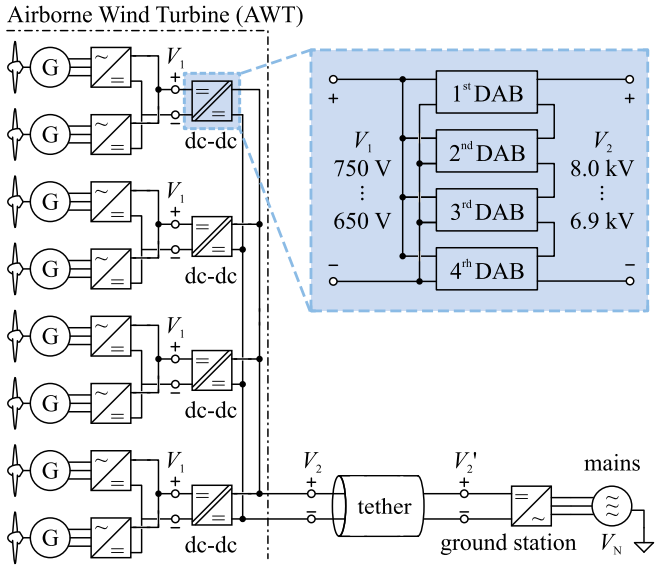


Fig. 1. Electrical system of the AWT. Four bidirectional dc–dc converters link eight voltage source rectifiers to a power transmission tether ($\approx 1$ km). The ground station, i.e., bidirectional dc–ac converter, connects the tether to the three-phase grid. Four single converter cells form a bidirectional dc–dc converter with a dc port voltage $V_2$ of up to 8 kV.

($650\ \mathrm{V} < V_1 < 750\ \mathrm{V}$) to a high tether voltage of up to 8 kV, cf., Fig. 1. The tether voltage is set to $V_2 = 8\ \mathrm{kV}\ V_1/750\ \mathrm{V}$, i.e., $V_2/V_1 = 8\ \mathrm{kV}/750\ \mathrm{V} \approx 10.7$, since the dc–dc converter is operated most efficiently with constant conversion ratio. The dc–dc converter further needs to allow for bidirectional energy transfer, in order to enable the startup of the AWT, where the rated power is 100 kW.

Fig. 1 depicts the electrical system of the AWT proposed in [1]: eight voltage source rectifiers convert the ac voltage of the generators to dc; four bidirectional dc–dc converters generate the high tether voltage; and the ground station connects the tether to the three-phase grid on the ground. The converter topology for the dc–dc converter is detailed in [2]. Each converter is formed by four single cells that are connected in parallel on the LV side and in series on the MV side, in order to reduce the maximum tether-side port voltage of each converter cell to 2 kV. Each converter cell essentially is a DAB converter with a FB circuit on the low-voltage side (dc port voltage $V_1$), a high-frequency transformer and inductor, and an NPC circuit on the MV side [dc port voltage $V_{2,i}$, see Fig. 2]. The optimization of the dc–dc converter with respect to minimum weight is particularly related to the optimization of the cooling system (heat sink plus fan), since the cooling system in a large part contributes to the total converter weight [1].

An optimization of heat sinks with respect to minimum weight, based on FEM, and a comparison of different materials suitable for low-weight heat sinks are presented in [3]. This optimization, however, considers only natural convection. Furthermore, the heat sink optimization presented in this work is part of an overall converter optimization procedure, and thus, analytical expressions for the expected thermal resistance (heat sink to ambient), rather than FEM simulation results, are desirable in order to increase the evaluation speed.

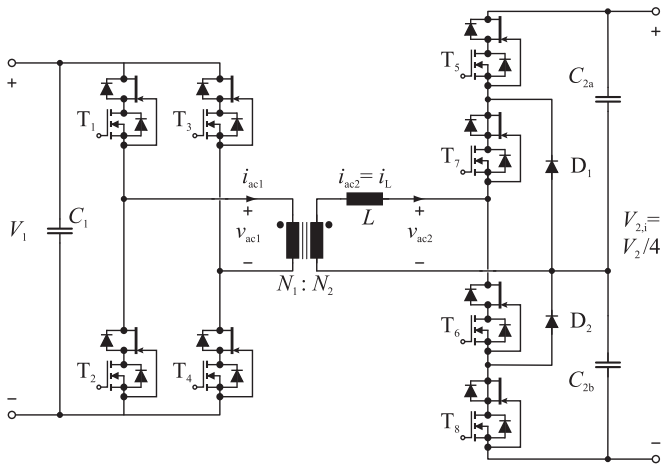


Fig. 2. Modified DAB converter topology used to realize a single cell of the bidirectional dc–dc converter [2].

Optimization procedures for complete cooling systems, with respect to minimum thermal resistance, are discussed in [4]–[7]. Lee, in [4], outlines the general optimization problem and the impacts of different parameter variations (e.g., fin thickness) on the resulting thermal resistance values. Holahan, in [5], refines the thermal model of the heat sink and includes the fan characteristic (static pressure versus volume flow) in the heat sink optimization. Finally, Drofenik *et al.*, in [6], present a complete heat sink optimization procedure. The optimizations in [5] and [6] minimize thermal resistance, in order to minimize the cooling system volume; the weight of the system is not considered. Ning *et al.* [7] were the first to present an optimization procedure considering the weight of the complete cooling system, i.e., fan plus heat sink. In [7], however, only heat sink–fan arrangements, which allow the airflow to bypass the heat sink, are considered. These arrangements are common in computer electronics cooling, where the airflow produced by the fan is channeled through the housing and only a fraction of the air flows through the heat sink channels. It has been shown in [4] that the lowest thermal resistance is achieved if the air is forced to flow through the heat sink channels.

This paper considers arrangements with ducted airflow from the fan through the heat sink channels, which creates a self-contained cooling system, common in cooling solutions for power electronics, and presents an optimization procedure that yields a minimum weight cooling system. It is based on analytical expressions and requires comparably low computational effort. Thus, the proposed procedure can directly be used as part of a complete converter weight optimization routine. Section II details the analytical cooling system model. Section III presents a comparison of the results obtained from FEM simulations, the model in [6], and the proposed analytical model. Section IV details the proposed optimization procedure. Section V, finally, discusses experimental results.

## II. Cooling System Model

Thermal modeling of a heat sink with a fan is a multiphysics problem. The thermal modeling involves three domains: heat conduction in solids, convective heat and mass transfers, and fluid dynamics. Fig. 3 illustrates the design process for any forced convection cooling system, considering two heat sinks a and b, which feature different geometries.[1] For a defined heat sink geometry, the fluid dynamic system impedance characteristic $\Delta p_{\mathrm{tot}}(\dot{V})$ is calculated. The impedance characteristic $\Delta p_{\mathrm{tot}}(\dot{V})$ correlates the static pressure difference between fluid inlet and outlet of the heat sink to the volume flow $\dot{V}$ through the heat sink. The fans, which are listed in Table I, provide a static pressure drop versus volume flow characteristic $\Delta p_{\mathrm{fan}}(\dot{V})$ (analogous to a nonideal voltage source). The intersection of the two characteristics, i.e.,

$$\Delta p_{\mathrm{fan}}(\dot{V}) - \Delta p_{\mathrm{tot}}(\dot{V}) = 0 \tag{1}$$

defines the volume flow $\dot{V}$ through the heat sink (analogous to a current through a resistor). The thermal resistance characteristic of the heat sink, $R_{\mathrm{th,S\text{-}a}}(\dot{V})$, may be calculated as a function of the volume flow $\dot{V}$ of the cooling fluid flowing through the system. As the volume flow $\dot{V}$ is obtained from (1) and, thus, is known, each cooling system, i.e., a combination of a heat sink and a fan, can be represented by means of an equivalent thermal resistance $R_{\mathrm{th,S\text{-}a}}$ that takes the temperature difference between the heat sink interface surface and the cooling fluid at the inlet into account.

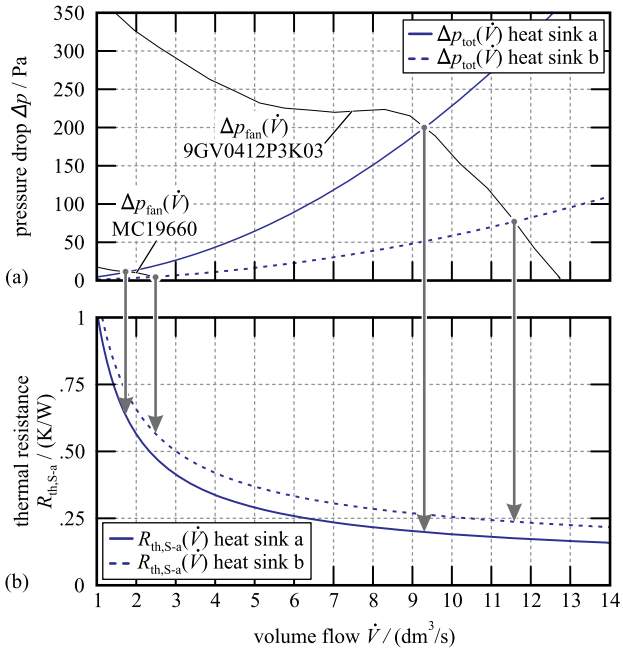


Fig. 3. Basic cooling system design process: the intersections of the heat sink impedances $\Delta p_{\mathrm{tot}}(\dot{V})$ of the heat sinks a and b with the characteristic of the selected fan determine the operating points, i.e., the volume flows $\dot{V}$, and the equivalent thermal resistances $R_{\mathrm{th,S\text{-}a}}$. (a) Characteristics of the fans MC19660 and 9GV0412P3K03, and the total system impedances $\Delta p_{\mathrm{tot}}(\dot{V})$ for two heat sink geometries a and b. (b) Thermal resistance characteristics $R_{\mathrm{th,S\text{-}a}}(\dot{V})$ of the two systems a and b as functions of volume flow $\dot{V}$. The heat sink geometries are $\{a, b\}$: $n = \{13, 9\}$, $c = \{25, 36\}$ mm, $L = 100$ mm, $b = 40$ mm, $d = 4$ mm, and $t = 1$ mm (cf., Fig. 4).

[1]The dimensions of the two heat sink geometries are $\{a, b\}$ : $n = \{13, 9\}$, $c = \{25, 36\}$ mm, $L = 100$ mm, $b = 40$ mm, $d = 4$ mm, and $t = 1$ mm (cf., Fig. 4).

TABLE I
40 mm × 40 mm AXIAL FANS CONSIDERED IN THE OPTIMIZATION

| Name | $\frac{P_{fan}}{W}$ | $\frac{L_{fan}}{mm}$ | $\frac{m_{fan}}{g}$ | $\frac{\dot{V}_{max}}{dm^3/s}$ | $\frac{\Delta p_{max}}{Pa}$ |
|---|---|---|---|---|---|
| GM0504PEV2-8.GN | 0.4 | 6 | 7.5 | 2.6 | 20.0 |
| MC19660 | 0.5 | 6 | 7.5 | 2.8 | 25.0 |
| BP402012H-W | 1.9 | 20 | 40.0 | 4.0 | 51.7 |
| 1608VL-04W-B60-B00 | 1.6 | 20 | 40.0 | 5.4 | 99.3 |
| 412JHH | 3.3 | 25 | 50.0 | 6.7 | 216.3 |
| 9L0412J301 | 3.7 | 28 | 55.0 | 8.5 | 205.1 |
| 9GA0412P6G001 | 2.8 | 20 | 35.0 | 7.1 | 319.2 |
| 9GV0412P3K03 | 10.1 | 28 | 50.0 | 12.7 | 416.2 |
| 1611FT-D4W-B86-B50 | 11.4 | 28 | 49.0 | 13.8 | 736.9 |
| 1619FT-04W-B86-B50 | 12.6 | 48 | 71.0 | 14.1 | 800.0 |

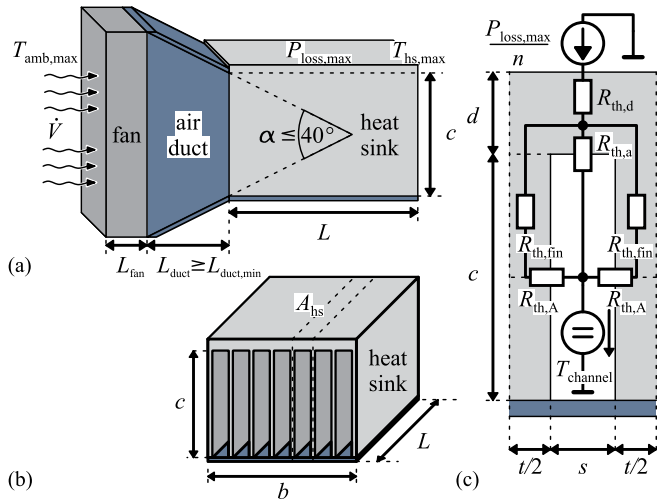


Fig. 4. (a) Cooling system model allowing for fin length optimization with air duct and bottom plate (made of PVC), which prevents airflow bypass. For the air duct, a maximum angle $\alpha \leq 40°$ and a minimum duct length $L_{\mathrm{duct}} \geq L_{\mathrm{duct,min}}$ is considered. (b) Geometrical model of the heat sink. The dotted lines indicate the symmetry axes used for the thermal model. (c) Heat sink thermal model. Due to symmetry properties, only two half-fins with thicknesses $t/2$, left and right channel walls, and one channel with height $c$ and width $s$ need to be considered [6].

Section II-A covers heat conduction and convective heat and mass transfers required for the calculation of $R_{\mathrm{th,S\text{-}a}}(\dot{V})$, and Section II-B covers the fluid dynamics required for the calculation of $\Delta p_{\mathrm{tot}}(\dot{V})$.

The proposed optimization procedure in Section IV considers a cooling system with a heat sink and a fan and extends a conventional heat sink geometry, as defined in Fig. 4(b), with an air duct, as shown in Fig. 4(a). It further considers closed heat sink channels, in order to avoid degradation of the heat sink's thermal resistance due to flow bypass [4]. The considered thermal model, as depicted in Fig. 4(c), assumes equal fin spacing $s$ and fin thickness $t$ with $n$ channels. Therefore, and due to symmetry conditions, only one channel/fin is modeled.

### A. Thermal Model

A simple way to model the 3-D heat conduction problem is to represent the 3-D structure as a network of thermal resistances. To keep the thermal network as simple as possible, the heat sink symmetries can be exploited, resulting in a thermal resistance network, as shown Fig. 4(c). Solving the resistive network results in a total thermal resistance of

$$\begin{aligned} R_{\mathrm{th,S\text{-}a}} &= R_{\mathrm{th},d} + \frac{1}{n}\frac{(R_{\mathrm{th,fin}} + R_{\mathrm{th,A}})R_{\mathrm{th,a}}}{R_{\mathrm{th,fin}} + R_{\mathrm{th,A}} + 2R_{\mathrm{th,a}}} \\ &= R_{\mathrm{th},d} + R_{\mathrm{th,conv}} \end{aligned} \tag{2}$$

and radiation is neglected. Based on the assumption of a uniform loss distribution across the heat sink base plate area $A_{\mathrm{hs}} = bL$, the thermal resistance $R_{\mathrm{th},d}$ is a function of the heat sink geometry and the heat sink material's thermal conductivity $\lambda_{\mathrm{hs}}$, i.e.,

$$R_{\mathrm{th},d} = \frac{d}{A_{\mathrm{hs}}\lambda_{\mathrm{hs}}}. \tag{3}$$

The temperature in the heat sink channels $T_{\mathrm{channel}}$ and the thermal resistances $R_{\mathrm{th,fin}}$, $R_{\mathrm{th,A}}$, and $R_{\mathrm{th,a}}$ depend on the volume flow, the geometry, and the position along the longitudinal axis of the channel. According to [8] and [9], these dependencies can be accurately modeled with the single fluid heat exchanger model that summarizes the thermal resistances, $R_{\mathrm{th,fin}}$, $R_{\mathrm{th,A}}$, and $R_{\mathrm{th,a}}$ in a single convective thermal resistance

$$R_{\mathrm{th,conv}} = \left[\rho_{\mathrm{air}} c_{\mathrm{air}} \dot{V}\left(1 - e^{-\frac{hA_{\mathrm{eff}}}{\rho_{\mathrm{air}} c_{\mathrm{air}} \dot{V}}}\right)\right]^{-1} \tag{4}$$

with the effective convective surface area $A_{\mathrm{eff}}$ and the fin efficiency $\eta$ [10]

$$A_{\mathrm{eff}} = n(2c\eta + s)L \text{ with } \eta = \frac{\tanh\left(\sqrt{\frac{2h(t+L)}{\lambda_{\mathrm{hs}} tL}} \cdot c\right)}{\sqrt{\frac{2h(t+L)}{\lambda_{\mathrm{hs}} tL}} \cdot c} \tag{5}$$

and with the average heat transfer coefficient $h$, cf., (15), being known. The average heat transfer coefficient is predominantly a function of the fluid boundary layer velocity [9]. For viscous flow in ducts, this boundary layer velocity is a function of the average fluid velocity in the duct and the fluid viscosity $\nu_{\mathrm{air}}$, which is generally described by means of a nondimensional analysis and the use of the Nusselt number, which represents the ratio of convective to conductive heat transfer [9]. The Nusselt number, however, is a function of average ducted fluid velocity, duct geometry, and the fluids Prandtl number (Pr). Muzychka and Yovanovich have derived an analytical model for the Nusselt number ($\mathrm{Nu}_{\sqrt{A}}$) suitable for the extruded-fin heat sink model, which includes the effect of flow development at the inlet of a duct with arbitrary cross section [11], as follows:

$$\mathrm{Nu}_{\sqrt{A}} = \left[\left(\frac{C_4 f(\mathrm{Pr})}{\sqrt{z^\star}}\right)^m + \left(\left\{C_1\left(\frac{f\mathrm{Re}_{\sqrt{A}}}{8\sqrt{\pi}\epsilon^\gamma}\right)\right\}^5 + \left\{C_2 C_3\left(\frac{f\mathrm{Re}_{\sqrt{A}}}{z^\star}\right)^{\frac{1}{3}}\right\}^5\right)^{\frac{m}{5}}\right]^{\frac{1}{m}}. \tag{6}$$

The required coefficients $C_1$, $C_2$, $C_3$, $C_4$, $\gamma$, and functions $f(\mathrm{Pr})$, $f\mathrm{Re}_{\sqrt{A}}$, $z^\star$, $\epsilon$, and $m$, as provided in [11], are summarized below.

At the inlet of the heat channel, the velocity profile at the boundary layer, i.e., the channel walls, shows a distinct dependence on the position along the longitudinal axis of the channel. As a consequence, the Nusselt number is large at the inlet of the duct, where the boundary layer velocity is large, i.e., the heat transfer coefficient $h$ will be large. The Nusselt number decreases along the thermal entry length, e.g., [9], and settles to a constant value. The model developed in [11] describes this effect and is solved for UWF and UWT boundary conditions. This model also accounts for the aspect ratio $\epsilon$ of the heat sink channels and is valid for any aspect ratio $\epsilon$, cf., (12). The models employed in [6] and [7] are approximations of the Nusselt number for viscous fluid flow between two parallel plates, which are only valid for aspect ratios $\epsilon \ll 1$.

The presented investigation assumes UWT, due to the high thermal conductivity of the heat sink material. For UWT boundary conditions, the function $f(\mathrm{Pr})$ is given by

$$f(\mathrm{Pr}) = \frac{0.564}{\left[1 + \left(1.664\,\mathrm{Pr}^{\frac{1}{6}}\right)^{\frac{9}{2}}\right]^{\frac{2}{9}}} \tag{7}$$

and the parameters $C_1$ and $C_3$ are given in [11] as

$$C_1 = 3.24 \text{ and } C_3 = 0.409. \tag{8}$$

To calculate the average (not local) Nusselt number, the parameters $C_2$ and $C_4$ are given by

$$C_2 = \frac{3}{2} \text{ and } C_4 = 2. \tag{9}$$

The shape parameter is given by

$$\gamma = -\frac{3}{10} \tag{10}$$

for rectangular ducts. The blending parameter $m$ is given by

$$m = 2.27 + 1.65\,\mathrm{Pr}^{\frac{1}{3}}. \tag{11}$$

The model in [11] is valid for $0.1 < \mathrm{Pr} < \infty$, which is valid for most heat exchanger applications. For the extruded-fin heat sink, the shape functions are given by

$$z^\star = \frac{L n \nu_{\mathrm{air}}}{\mathrm{Pr}\cdot\dot{V}} \text{ and } \epsilon = \begin{cases} \frac{s}{c}, & \text{if } s \le c \\ \frac{c}{s}, & \text{if } s > c. \end{cases} \tag{12}$$

The friction factor Reynolds product function

$$f\mathrm{Re}_{\sqrt{A}} = \left[\frac{11.8336\cdot\dot{V}}{L n \nu_{\mathrm{air}}} + \left(f\mathrm{Re}_{\sqrt{A},\mathrm{fd}}\right)^2\right]^{\frac{1}{2}} \text{ with} \tag{13}$$

$$f\mathrm{Re}_{\sqrt{A},\mathrm{fd}} = \frac{12}{\sqrt{\epsilon}(1+\epsilon)\left[1 - \frac{192}{\pi^5}\epsilon\tanh\left(\frac{\pi}{2\epsilon}\right)\right]} \tag{14}$$

describes the effect of the boundary layer velocity profile on the mass transfer [15]. With this and with (6), the heat transfer coefficient becomes

$$h = \frac{\mathrm{Nu}_{\sqrt{A}}\lambda_{\mathrm{air}}}{d_h} \text{ with } d_h = \frac{2sc}{s+c} \text{ and } s = \frac{b-(n+1)t}{n}. \tag{15}$$

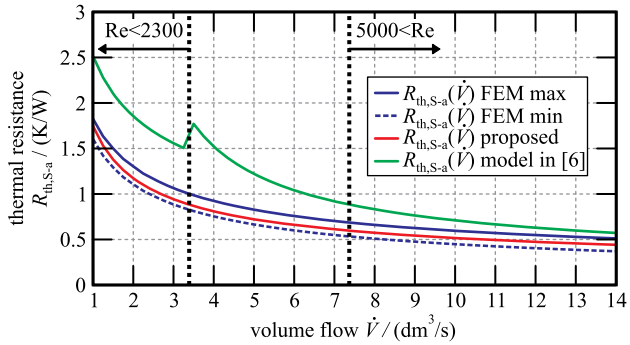


Fig. 5. Thermal resistance $R_{\mathrm{th,S\text{-}a}}$ as a function of volume flow $\dot{V}$: FEM calculated with maximum base plate temperature (at the fluid outlet, solid blue), FEM calculated with minimum base plate temperature (at the fluid inlet, dotted blue), proposed model (red), and model proposed in [6] (green), for a heat sink with dimensions $n = 5$, $L = 100$ mm, $b = 40$ mm, $d = 3$ mm, $c = 30$ mm, and $t = 1$ mm, cf., Fig. 4.

Expression (15) enables the total thermal resistance (2) to be calculated as a function of geometry and volume flow.

Fig. 5 shows the thermal resistances as functions of the volume flow for a particular heat sink calculated with the model in [6] (green line), the proposed model (red line), and FEM simulation. The FEM simulated thermal resistances are calculated from the maximum base plate temperatures (at the fluid outlet, solid blue line) and the minimum base plate temperatures (at the fluid inlet, dotted blue line). A comparison reveals that the model in [6] significantly overestimates the thermal resistance for low volume flows. The discontinuity in the model given in [6] is caused by the discrete distinction between laminar $(\mathrm{Re} < 2300)$ and turbulent $(\mathrm{Re} > 5000)$ flow and the use of the turbulent flow model within the transition region $(2300 < \mathrm{Re} < 5000)$. The distinction between turbulent and laminar flow is essential for fully developed fluid flow. This distinction, however, only becomes valid once the fluid dynamic entry length has been reached, where the fluid flow turns from laminar to turbulent [12]. For the cooling system geometry in Fig. 5, the fluid dynamic entry length [9]

$$L_h = \frac{L_h^+}{\sqrt{A}}\mathrm{Re}_{\sqrt{A}} = L_h^+\frac{\dot{V}}{n\nu_{\mathrm{air}}} \tag{16}$$

with the dimensionless fluid dynamic entry length for laminar flow [9]

$$L_h^+ = 0.0822\epsilon(1+\epsilon)^2\left[1 - \frac{192\epsilon}{\pi^5}\tanh\left(\frac{\pi}{2\epsilon}\right)\right] \tag{17}$$

is $L_h = 650$ mm at $\mathrm{Re} = 2300$ and $L_h = 1425$ mm at $\mathrm{Re} = 5000$. Therefore, turbulent flow will not develop over the whole length $L = 100$ mm $\ll L_h$ of the heat sinks presented in this work.

### *B. Fluid Dynamic Model*

The sole purpose of the fluid dynamic model is to determine the volume flow $\dot{V}$, which is an input of the thermal model [in particular (4)] and generated by the selected fan. Literature review reveals that different phenomena affect the relation between the total static pressure drop $\Delta p_{\mathrm{tot}}$ and the volume flow,

for a given heat sink. All these effects are functions of geometry and average air speed. In [6], only the apparent friction factor, $f_{\text{app}}$, is considered and approximated as the friction factor for fully developed fluid flow between two parallel plates, which turns out to insufficiently predict the actual pressure drop and volume flow. The apparent friction factor $f_{\text{app}}$ is approximately the same as the friction factor for fully developed fluid flow if the duct length is greater than ten times the fluid dynamic entry length, i.e., $L \gtrapprox 10L_h$ [9], which, however, is not fulfilled in commonly used heat sink geometries. Improved fluid dynamic models are proposed in [13]–[15]. Shabany [13] and Culham *et al.* [14] include the effects of sudden contraction at the inlet and sudden expansion at the outlet, based on [12], and the effects of developing fluid flow [15]. In addition, the conservation of momentum needs to be considered, in order to account for the fluid acceleration in the air duct and the heat sink. Respective literature is found in [12], [16]–[18].

The total cooling system static pressure drop is the sum of all the pressure drop contributions expressed as functions of the volume flow, i.e.,

$$\Delta p_{\text{tot}}(\dot{V}) = \Delta p_{\text{hs}}(\dot{V}) + \Delta p_{\text{duct}}(\dot{V}) + \Delta p_{\text{acc}}(\dot{V}) \tag{18}$$

with $\Delta p_{\text{hs}}$, $\Delta p_{\text{duct}}$, and $\Delta p_{\text{acc}}$ denoting the static pressure drop due to fluid friction of the heat sink ($\Delta p_{\text{hs}}$), due to fluid friction of the air duct ($\Delta p_{\text{duct}}$), and due to frictionless fluid flow acceleration ($\Delta p_{\text{acc}}$), respectively.

The pressure drop $\Delta p_{\text{hs}}$, i.e.,

$$\Delta p_{\text{hs}}(\dot{V}) = \left( f_{\text{app}}(\dot{V}) \frac{L}{d_h} + K_{\text{se}} + K_{\text{sc}} \right) \cdot \frac{\rho}{2} \overline{U}^2_{\text{hs}}(\dot{V}) \tag{19}$$

consists of the friction factors for sudden contraction and sudden expansion [12], [13], [18], i.e.,

$$K_{\text{se}} = \left(1 - \frac{d_h^2}{D_h^2}\right)^2 = \left(1 - \left(1 - \frac{(n+1)t}{b}\right)^2\right)^2 \tag{20}$$

$$K_{\text{sc}} \approx 0.42 \left(1 - \frac{d_h^2}{D_h^2}\right) = 0.42 \left(1 - \left(1 - \frac{(n+1)t}{b}\right)^2\right) \tag{21}$$

and the apparent friction factor for viscous fluid flow in ducts with arbitrary cross sections [15], i.e.,

$$f_{\text{app}}(\dot{V}) = \frac{f\text{Re}_{\sqrt{A}}(\dot{V})}{\text{Re}_{\sqrt{A}}(\dot{V})} = \frac{n\nu_{\text{air}}\sqrt{cs}}{\dot{V}} \cdot f\text{Re}_{\sqrt{A}}(\dot{V}). \tag{22}$$

Noteworthy to mention at this point is the importance of the friction factor Reynolds product $f\text{Re}_{\sqrt{A}}(\dot{V})$ [cf., (13)]. The friction factor Reynolds product appears in both the thermal (6) and the fluid dynamic models (19) because it describes the interactions between the fluid in motion and the channel walls. An increase in $f\text{Re}_{\sqrt{A}}(\dot{V})$ denotes an increase in mass transfer, which results in a greater heat transfer, i.e., $\text{Nu}_{\sqrt{A}}$ increases, but also an increase in the friction at the channel walls. Consequently, a direct tradeoff between heat transfer and required pressure drop exists, as an increased mass transfer simultaneously increases the heat transfer coefficient $h$ and the apparent friction factor $f_{\text{app}}$, cf., (15) and (22).

The pressure drop $\Delta p_{\text{duct}}$

$$\Delta p_{\text{duct}}(\dot{V}) = \left( f_{\text{app,duct}}(\dot{V}) \frac{L_{\text{duct}}}{\overline{d}_{h,\text{duct}}} \frac{1}{4} + K_{\text{venturi}} \right) \cdot \frac{\rho}{2} \overline{U}^2_{\text{duct}}(\dot{V}) \tag{23}$$

consists of the apparent friction factor for the average duct hydraulic diameter $f_{\text{app,duct}}$ [15] and the friction factor for a venturi nozzle $K_{\text{venturi}}$ [12], i.e.,

$$f_{\text{app,duct}}(\dot{V}) = \frac{\nu_{\text{air}}\sqrt{b(b+c)}}{\sqrt{2}\dot{V}} \cdot \left[ \frac{11.8336\dot{V}}{L_{\text{duct}}\nu_{\text{air}}} + \left( f\text{Re}_{\sqrt{A},\text{fd}} \right)^2 \right]^{\frac{1}{2}}, \tag{24}$$

$$\begin{aligned} \overline{d}_{h,\text{duct}} &= \frac{2b(b+c)}{3b+c} \\ L_{\text{duct}} &= \max\left[ \frac{b-c}{2\tan(\alpha)}, L_{\text{duct,min}} \right] \end{aligned} \tag{25}$$

$$\epsilon_{\text{duct}} = \frac{b+c}{2c}, \text{ and } \quad K_{\text{venturi}} \approx 0.2. \tag{26}$$

A minimal air duct length $L_{\text{duct,min}}$ is recommended, since the commonly used assumption that the fan produces an evenly distributed laminar inflow pattern cannot be true because no air can flow through the hub of the fan. The airflow and pressure distributions produced by the fan require a certain air duct length to form the assumed inflow conditions. The influence of this fan system effect, however, is poorly documented, but commercially available products reveal its importance, e.g., the only difference between the cooling aggregates LA 6 and LA V 6, manufactured by Fischer Elektronik, is a 3-cm air duct between the fan and the heat sink, but this air duct reduces the thermal resistance by approximately 13%. This work considers a minimal duct length of $L_{\text{duct,min}} = 3$ cm, in order to reduce the degradation of the fan static pressure drop characteristic, i.e., $\Delta p_{\text{fan}}$, due to fan system effects. The friction factor for the venturi nozzle $K_{\text{venturi}}$ is a function of the air duct shape and increases with the duct angle $\alpha$, i.e., $K_{\text{venturi}} \in [0.04, 0.5]$ [12]. In this paper, an air duct angle of $0 \leq \alpha \leq 40^\circ$ is considered, and thus, the contribution of $\Delta p_{\text{duct}}$ to the total static pressure drop $\Delta p_{\text{tot}}$ is small. However, without an air duct, i.e., if the fan is directly mounted to the heat sink, the static pressure drop generated by the fan may be considerably reduced.

The average velocities of the cooling fluid are given as functions of the volume flow, i.e.,

$$\overline{U}_{\text{hs}}(\dot{V}) = \frac{\dot{V}}{nsc} \text{ and } \overline{U}_{\text{duct}}(\dot{V}) = \frac{\dot{V}}{bc}. \tag{27}$$

Conservation of momentum for the cooling fluid flowing through the air duct and the heat sink [12], [16]–[18] gives the pressure drop for the frictionless fluid flow acceleration, i.e.,

$$\Delta p_{\text{acc}}(\dot{V}) = \left[ \frac{1}{(nsc)^2} - \frac{1}{b^4} \right] \frac{\rho}{2} \dot{V}^2. \tag{28}$$

Fig. 6(a) shows the contributions of the different effects causing the total cooling system static pressure drop for an

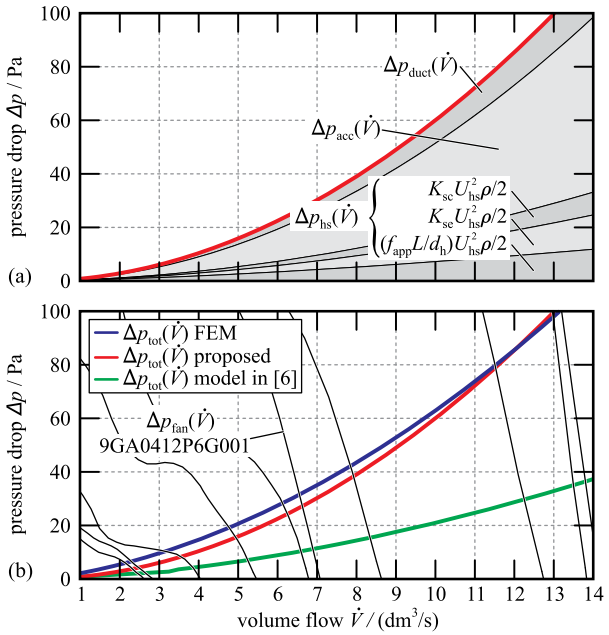


Fig. 6. Cooling system static pressure drop $\Delta p_{\mathrm{tot}}$ as a function of volume flow $\dot{V}$: (a) the shaded areas from bottom to top show the contributions of apparent friction factor $f_{\mathrm{app}}$, sudden expansion $K_{\mathrm{se}}$, sudden contraction $K_{\mathrm{sc}}$, conservation of momentum $\Delta p_{\mathrm{acc}}$, and the friction of the air duct $\Delta p_{\mathrm{duct}}$; (b) FEM simulation results (blue), proposed model (red), and model in [6] (green). The solid black lines denote the static pressure drop characteristics of the fans listed in Table I. The heat sink dimensions are $n = 5$, $L = 100$ mm, $b = 40$ mm, $d = 3$ mm, $c = 30$ mm, and $t = 1$ mm.

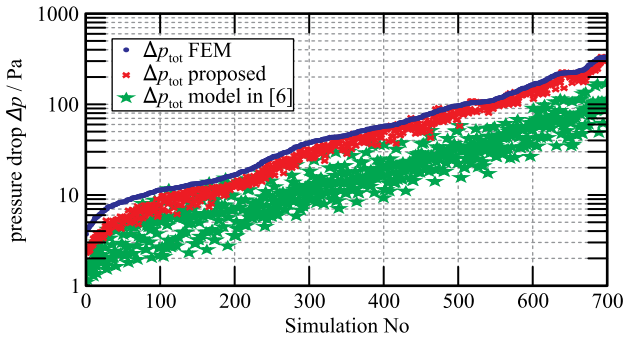


Fig. 7. Comparison of the total static pressure drop $\Delta p_{\mathrm{tot}}$ at the operating points of the fans listed in Table I. The geometry parameters of the considered cooling systems are in the range of $L \in [60\ \mathrm{mm}, 100\ \mathrm{mm}]$, $n \in [5, 13]$, $c \in [10\ \mathrm{mm}, 37\ \mathrm{mm}]$, $b = 40$ mm, and $t = 1$ mm. Blue dots: FEM simulation results, green dots: results calculated with the cooling system model in [6], and red crosses: proposed cooling system model.

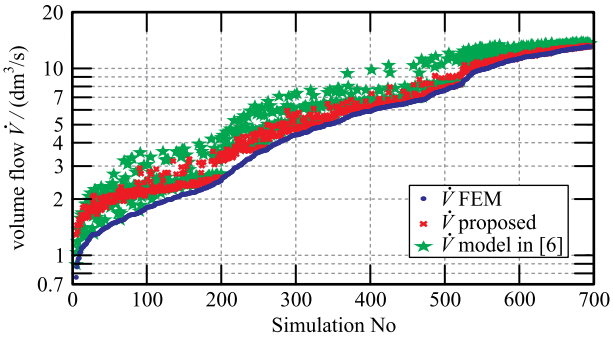


Fig. 8. Comparison of the static volume flows $\dot{V}$ at the operating points of the fans listed in Table I. The geometry parameters of the considered cooling systems are in the range of $L \in [60\ \mathrm{mm}, 100\ \mathrm{mm}]$, $n \in [5, 13]$, $c \in [10\ \mathrm{mm}, 37\ \mathrm{mm}]$, $b = 40$ mm, $t = 1$ mm. Blue dots: FEM simulation results, green dots: results calculated with the cooling system model in [6], and red crosses: proposed cooling system model.

example cooling system with dimensions: $n = 5$, $L = 100$ mm, $b = 40$ mm, $d = 3$ mm, $c = 30$ mm, and $t = 1$ mm. The shaded areas from bottom to top are the contributions of the following effects: apparent friction $f_{\mathrm{app}}$, sudden expansion $K_{\mathrm{se}}$, sudden contraction $K_{\mathrm{sc}}$, conservation of momentum $\Delta p_{\mathrm{acc}}$, and friction of the duct $\Delta p_{\mathrm{duct}}$.

Fig. 6(b) shows the total static pressure drop as a function of the volume flow calculated with the proposed fluid dynamic model (red line), the fluid dynamic model in [6] (with fitting factor $k$, green line), and FEM simulation results (blue line).

## III. Model Comparison

The results obtained with the proposed thermal and fluid dynamic model and the model in [6] are compared to FEM simulation results and experimental results (in Section V), in order to present the improvements achieved with the analytical model. Based on the assumption that the most accurate calculations of thermal resistance, volume flow, and pressure drop are feasible with FEM simulations, a large number of FEM simulations is used as basis for the evaluation.

The utilized 3-D FEM simulation software is COMSOL Multiphysics. Exploiting all symmetries, only half a fin and half a channel is modeled. The Conjugate Heat Transfer (ntif) module is used with Air and Aluminum provided in the standard library. The boundary conditions for the fluid dynamic problem are as follows: "no slip" at the heat sink channel wall, "symmetry" at the channel midplane, "symmetry" in the air duct at the channel midplane and the fin midplane, "pressure, no viscous stress" at the channel outlet, and "laminar inflow" enforcing a flow rate of $\dot{V}/(2n)$ at the fan inlet. The boundary conditions for the heat transfer in solids are as follows: a "total heat flux" of $80\ \mathrm{W}/(2n)$ at the base plate surface, "symmetry" at the channel midplane, "symmetry" at the fin midplane, an "inflow heat flux" of $0\ \mathrm{W/m^2}$ with an external temperature of 30 °C at the fan inlet, and the "outflow" at the channel outlet. The mesh settings are "physics-controlled mesh" with a "coarse" element size. The study is a "parametric sweep" of the parameter volume flow $\dot{V} \in [1, 14]\ \mathrm{dm^3/s}$, with a linear step size of $0.25\ \mathrm{dm^3/s}$. From the "parametric sweep", the heat sink system characteristics $\Delta p_{\mathrm{tot}}(\dot{V})$ and $R_{\mathrm{th,S\text{-}a}}(\dot{V}) = (T_{\mathrm{hs,max}} - 30\ ^\circ\mathrm{C})/80\ \mathrm{W}$ are extracted, where $T_{\mathrm{hs,max}}$ is the maximum temperature on the base plate surface.

The fluid dynamic models, which determine the operating point of the fan, are needed to evaluate the thermal model, in particular (4), and are discussed first. Figs. 7 and 8 show the operating points calculated for all combinations of all ten considered fans in Table I and 72 different heat sink geometries with parameters in the range of $L \in [60\ \mathrm{mm}, 100\ \mathrm{mm}]$, $n \in [5, 13]$, $c \in [10\ \mathrm{mm}, 37\ \mathrm{mm}]$, $b = 40$ mm, $t = 1$ mm, and $\dot{V} \in [1\ \mathrm{dm^3/s}, 14\ \mathrm{dm^3/s}]$, i.e., 720 different cooling systems. The operating point is determined by equalizing the cooling system static pressure drop and the fan characteristic (the fan characteristics are obtained from data sheets). In Figs. 7–10

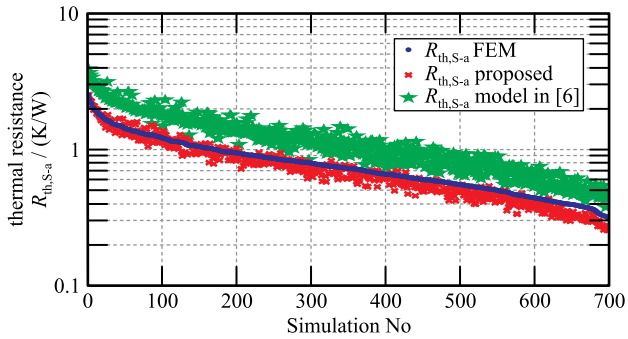


Fig. 9. Comparison of the thermal resistance values $R_{\text{th,S-a}}$ at the operating points of the fans, as listed in Table I, being determined by the FEM fluid dynamic model. The geometry parameters of the considered cooling systems are in the range of $L \in [60\text{ mm}, 100\text{ mm}]$, $n \in [5, 13]$, $c \in [10\text{ mm}, 37\text{ mm}]$, $b = 40$ mm, and $t = 1$ mm. Blue dots: FEM simulation results, green dots: results calculated with the cooling system model in [6], and red crosses: proposed cooling system model.

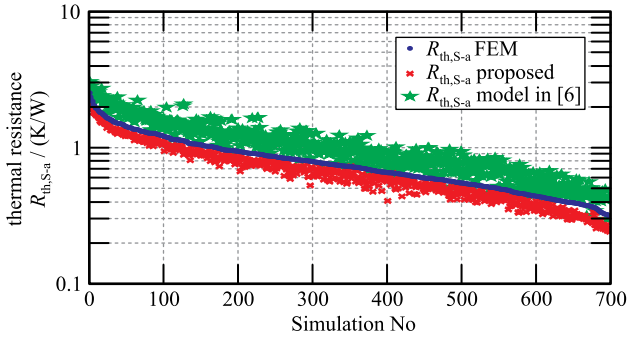


Fig. 10. Comparison of the thermal resistance values $R_{\text{th,S-a}}$ at the operating points of the fans, as listed in Table I, being determined by the corresponding fluid dynamic models. The geometry parameters of the considered cooling systems are in the range of $L \in [60\text{ mm}, 100\text{ mm}]$, $n \in [5, 13]$, $c \in [10\text{ mm}, 37\text{ mm}]$, $b = 40$ mm, and $t = 1$ mm. Blue dots: FEM simulation results, green dots: results calculated with the cooling system model in [6], and red crosses: proposed cooling system model.

and 14, the results of the FEM simulations are marked with blue dots, the results of the proposed model with red crosses, and the results of the model in [6] with green stars. For a better graphic representation, the results in Figs. 7–10 are sorted in different orders, such that the blue line (FEM simulation results) is monotonic.

Fig. 7 shows a high correlation for the pressure drop of the proposed model and the FEM simulation with a mean deviation of

$$\sigma_{\Delta p_{\text{tot}}} = \frac{1}{k}\sum_{i=1}^{k}\frac{|\Delta p_{\text{tot,FEM},i} - \Delta p_{\text{tot,model},i}|}{\Delta p_{\text{tot,FEM},i}} = 21\% \quad (29)$$

$(k = 720)$, whereas the previous cooling system model in [6] gives a mean deviation of $\sigma_{\Delta p_{\text{tot}}} = 64.3\%$.

Fig. 8 shows the volume flows determined at the calculated operating points. The mean deviations between simulated and calculated results are 14.6% for the proposed model and 24.7% for the model detailed in [6].

Fig. 9 depicts the expected thermal resistances if the operating points are determined based on the pressure drop versus volume flow characteristics obtained by means of FEM simulations. This facilitates a direct comparison of the three thermal models and excludes the interaction of the fluid dynamic and thermal models. The mean deviations between simulated and calculated results are 9.9% for the proposed model and 45.7% for the previous model [6].

Fig. 10, finally, compares the expected thermal resistances of the combined fluid dynamic and thermal models. The mean deviations are 15% for the proposed model and 30.3% for the previous model [6].

## IV. Cooling System Optimization

### A. General Constrained Optimization Procedure

The algorithm of the optimization procedure, as illustrated in Fig. 11, yields a minimum weight cooling system and, additionally, satisfies design and manufacturability constraints. Its main input parameters are a list of considered fans, the required base plate area $A_{\text{hs}}$, and the maximum allowable thermal resistance of the cooling system, i.e.,

$$R_{\text{th,S-a,max}} = \frac{T_{\text{hs,max}} - T_{\text{amb,max}}}{P_{\text{loss,max}}} \quad (30)$$

with maximum base plate temperature of the heat sink ($T_{\text{hs,max}}$), maximum ambient temperature specified ($T_{\text{amb,max}}$), and maximum thermal flux transmitted to the heat sink's base plate ($P_{\text{loss,max}}$).

The thickness of the base plate is set to the minimum possible value, in order to achieve a low weight of the heat sink. In this paper, the minimum thickness is $d = 3$ mm, in order to facilitate sufficient mechanical stability and depth for the M3 threads that are needed to mount the components onto the heat sink. Despite the thin base plate, a constant and homogeneous temperature $T_{\text{hs,max}}$ all over the surface of the base plate is considered, due to the high thermal conductivity material, i.e., aluminum, employed. Moreover, the components mounted to the heat sink are assumed to cover large parts of the available surface, as shown in Fig. 13(a) and (b), in order to achieve a well-balanced distribution of the thermal flux across the surface of the base plate. The procedure detailed in [6] sets the width $b$ of the heat sink equal to the width of the fan employed. The air duct allows for a variable fin length $c$ and adds an additional degree of freedom. The presented procedure considers a height of the heat sink, i.e., $c + d$, equal to or less than the height of the fan. The total area requirement of all components (including any additional space for placement, e.g., due to isolation requirements) defines the length of the heat sink $L = A_{\text{hs}}/b$.

Thus, the variables remaining for optimization are as follows: the number of channels $n$, the fin thickness $t$, and the fin length $c$, which are constrained by the manufacturing technology available. The presented cooling systems are manufactured with computer numerical control machines and, thus, a minimum fin thickness of 1 mm and a minimum channel width $s$ of 1 mm apply.

In an initial step, the optimization procedure selects a list of fans. The fan list consists of fans with equal widths and contains the fan's width, height, weight, and pressure drop characteristic. Furthermore, the geometry parameters defined by the fan, i.e.,

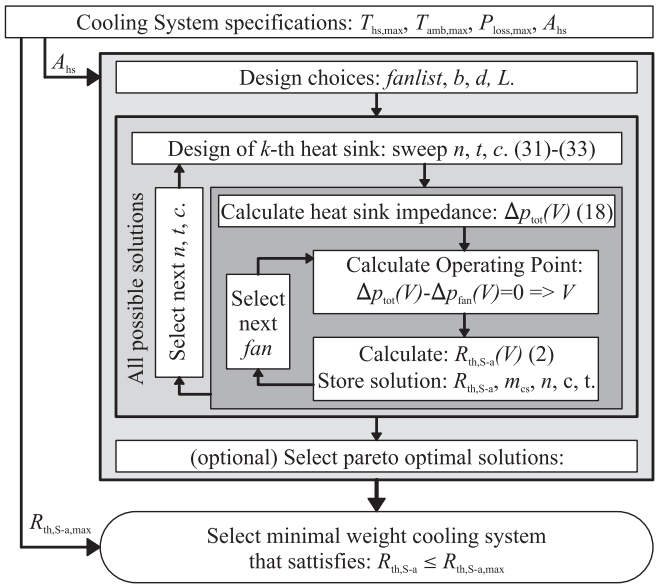


Fig. 11. Proposed cooling system optimization procedure for minimum weight cooling system that satisfies $R_{\mathrm{th,S\text{-}a}} \le R_{\mathrm{th,S\text{-}a,max}}$. The calculated weight $m_{\mathrm{cs}}$ is the sum of the weight of all the components, i.e., heat sink, fan, air duct, and bottom plate.

$b$ and $L$, are set. In a second step, an outer loop sweeps all possible heat sink geometries given by

$$1 \le n \le \left\lfloor \frac{b - t_{\min}}{s_{\min} + t_{\min}} \right\rfloor \quad (31)$$

$$t_{\min} \le t \le \frac{b - n s_{\min}}{n+1} \quad (32)$$

$$c_{\min} \le c \le b - c \quad (33)$$

where $c_{\min}$ can be chosen arbitrarily. With the heat sink and duct geometries defined, the fluid dynamic system impedance characteristic $\Delta p_{\mathrm{tot}}(\dot{V})$ is calculated. An inner loop calculates the operating point of the fan, the resulting thermal resistance $R_{\mathrm{th,S\text{-}a}}$, and the total weight $m_{\mathrm{cs}}$ of the particular combination of heat sink, fan, air duct, and bottom plate. The solutions are stored in a solution database.

To reduce the storage space of the solution database, all suboptimal solutions are excluded, i.e., all solutions that feature nonminimal thermal resistances $R_{\mathrm{th,S\text{-}a}}$ for a given mass $m_{\mathrm{cs}}$ are excluded. The algorithm, finally, picks that particular entry of the result database, which features minimum weight and satisfies $R_{\mathrm{th,S\text{-}a}} \le R_{\mathrm{th,S\text{-}a,max}}$. This entry represents the optimal cooling system design [within the constraints and accuracies resulting from the list of considered fans, cf., Table I, and the accuracies due to limited resolutions of the sweeps (32) and (33)].

The bidirectional dc–dc converter in [2] requires three cooling systems. The switches of the LV-side FB will dissipate 15 W each. The semiconductor switches feature a thermal junction to case resistance of 0.63 K/W, and the thermal resistance of the insulating thermal interface material between the TO-247 package case and the heat sink is 0.31 K/W. The maximum junction temperature is restricted to 120 °C, which translates into a maximum heat sink base plate temperature of $T_{\mathrm{hs,max}} = 106$ °C. Allowing for a maximum ambient temperature of $T_{\mathrm{amb,max}} = 40$ °C, the required thermal resistance becomes $R_{\mathrm{th,S\text{-}a,max,FB}} = 1.1$ K/W. The thermal resistance required for the MV NPC converter is calculated in an analogous manner and is $R_{\mathrm{th,S\text{-}a,max,NPC}} = 1.25$ K/W. The cooling system for transformer and inductor requires $R_{\mathrm{th,S\text{-}a,max,tr+ind}} = 0.46$ K/W. The minimum base plate areas for the FB and the NPC converters are both $A_{\mathrm{hs,min,FB}} = A_{\mathrm{hs,min,NPC}} = 2400$ mm$^2$; the minimum base plate area for the inductor and the transformer is $A_{\mathrm{hs,min,tr+in}} = 3200$ mm$^2$. Table II summarizes the respective optimization results.

TABLE II
OPTIMIZATION RESULTS. ($d = 3$ mm, $t \in [1\text{ mm}, 2\text{ mm}]$, $\delta t = 0.1$ mm, $c_{\min} = 10$ mm)

| | MV side NPC | LV side FB | Transformer and ind. |
|---|---|---|---|
| $R_{\mathrm{th,S\text{-}a,max}}$ | 1.25 K/W | 1.10 K/W | 0.46 K/W |
| $R_{\mathrm{th,S\text{-}a}}$ | 1.241 K/W | 1.097 K/W | 0.444 K/W |
| $m_{\mathrm{cs}}$ | 61 g | 65 g | 116 g |
| $n$ | 8 | 8 | 11 |
| $c$ | 17 mm | 20 mm | 17 mm |
| fan | MC19660 | MC19660 | 9GA0412P6G001 |
| $L$ | 60 mm | 60 mm | 80 mm |
| $b$ | 40 mm | 40 mm | 40 mm |
| $t$ | 1 mm | 1 mm | 1 mm |

### *B. Improvements Achieved With Variable Fin Length*

The cooling system in Fig. 3(a) adds an air duct between the fan and the heat sink and, thus, allows a variable fin length of the heat sink. An air duct built of lightweight materials can be beneficial, because a reduction in the fin length reduces the weight of the heat sink, decreases the average thermal resistance of the fin, $R_{\mathrm{th,fin}}$, and increases the velocity of the air inside the channels, which, in turn, increases the heat transfer coefficient $h$ between the aluminum channel walls and the air. A reduction in the fin length, however, reduces the effective surface of the fin, which counteracts the decrease in the thermal resistance between the fin and the air. The air duct, finally, causes an additional pressure drop and a slight increase in the total weight and the volume of the cooling system. With the model presented in Section II, the impact of a variable fin length on the thermal resistances of the heat sink can be easily analyzed.

Fig. 12(a) depicts the total weights of optimized cooling systems with $A_{\mathrm{hs}} = 40$ mm $\times$ 60 mm, a constant fin length of $c_{\min} = 37$ mm for four different fans, and different values of $R_{\mathrm{th,S\text{-}a,max}}$; steps occur in the plots as a result of the discrete number of channels $n$. According to these results, the low-power fans (MC19660 and GM0504PEV2-8.GN) yield lighter cooling systems for $R_{\mathrm{th,S\text{-}a,max}} > 0.6$ K/W due to the lower weights of the fans. These fans, however, fail to realize cooling systems with low thermal resistances, i.e., no solutions result for $R_{\mathrm{th,S\text{-}a,max}} > 0.5$ K/W, due to limited airflow capabilities. The fans 9GA0412P6G001 ($P_{\mathrm{fan}} = 2.76$ W) and 1611FT-D4W-B86-B50 ($P_{\mathrm{fan}} = 11.4$ W) cause the total weight to

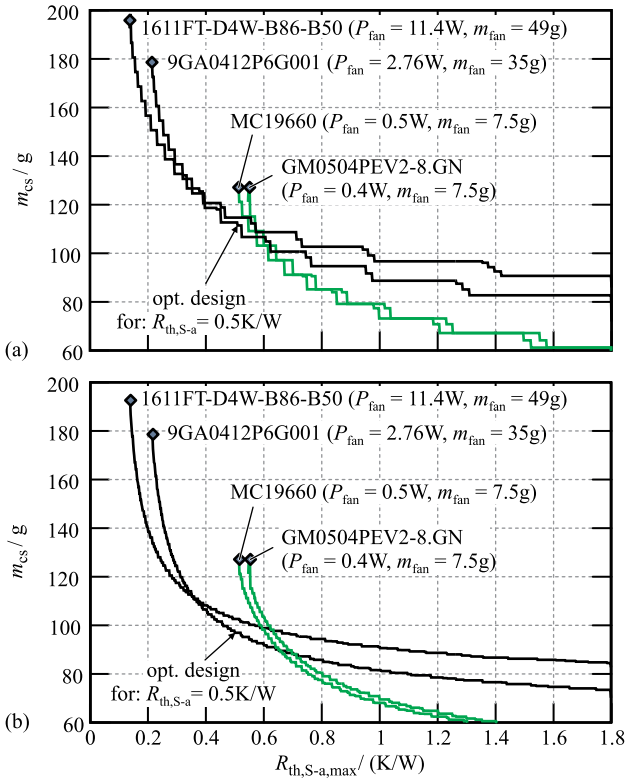


Fig. 12. Optimization results for $R_{\mathrm{th,S\text{-}a,max}} \in [0, 1.8]$ K/W considering four fans, $A_{\mathrm{hs}} = 40$ mm $\times$ 60 mm, and $d = 3$ mm. (a) Fin length constrained to $c = 37$ mm. (b) Optimal fin length selected.

increase for $R_{\mathrm{th,S\text{-}a,max}} > 0.6$ K/W and are, thus, better suited for low maximum thermal resistances $R_{\mathrm{th,S\text{-}a,max}} < 0.6$ K/W.

Fig. 12(b) shows the total weights of the same cooling systems with the optimal fin lengths being selected. The extended cooling system model clearly indicates the combination of heat sink and fan, which results in the minimum weight cooling system, e.g., the 9GA0412P6G001 fan is the optimal combination for $0.35$ K/W $< R_{\mathrm{th,S\text{-}a,max}} < 0.65$ K/W. A comparison between Fig. 12(a) and (b) reveals the weight reduction achievable with the extended cooling system model, e.g., for $R_{\mathrm{th,S\text{-}a,max}} = 0.5$ K/W, the total weight is reduced by 14% (97 g instead of 113 g).

## V. Experimental Results

Twelve experimental cooling systems, as listed in Table III, are used to verify the theoretical considerations presented earlier. The twelve cooling systems consist of three different heat sinks featuring the same base plate thicknesses $d = 3$ mm and fin breaths $t = 1$ mm. The heat sinks differ in length, fin length, and number of channels $\{L, c, n\} = \{\{60$ mm, 37 mm, $8\}, \{60$ mm, 25 mm, $9\}, \{80$ mm, 37 mm, $13\}\}$. The thermal resistances are measured for each combination of the three heat sinks and four different fans (GM0504PEV2-8.GN, MC19660, 9GA0412P6G001, and 1611FT-D4W-B86-B50) to obtain twelve cooling systems.

Four 100-$\Omega$ resistors are mounted to the base plates of each heat sink, in order to provide defined heat fluxes. The base plate temperatures $T_{\mathrm{hs}}$ are measured at the surfaces, as indicated in Fig. 13(a) and (b), with type-$K$ thermocouples. The cooling system is mounted on a hollow cardboard box and covered with thermally insulating material, to reduce measurement errors due to heat conduction to the supporting table, natural convection, and radiation.

TABLE III
Experimental Cooling Systems ($d = 3$ mm, $t = 1$ mm)

| heat sink dimensions | | | |
|---|---|---|---|
| Fin length $c$ | 37 mm | 25 mm | 37 mm |
| Heat sink length $L$ | 60 mm | 60 mm | 80 mm |
| Number of channels $n$ | 8 | 9 | 13 |
| 40 mm $\times$ 40 mm axial fan | cooling system number | | |
| GM0504PEV2-8.GN | 1 | 5 | 9 |
| MC19660 | 2 | 6 | 10 |
| 9GA0412P6G001 | 3 | 7 | 11 |
| 1611FT-D4W-B86-B50 | 4 | 8 | 12 |

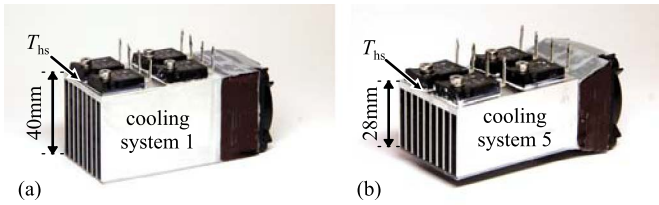


Fig. 13. Pictures of the realized cooling systems. $T_{\mathrm{hs}}$ indicates the location for the temperature measurement.

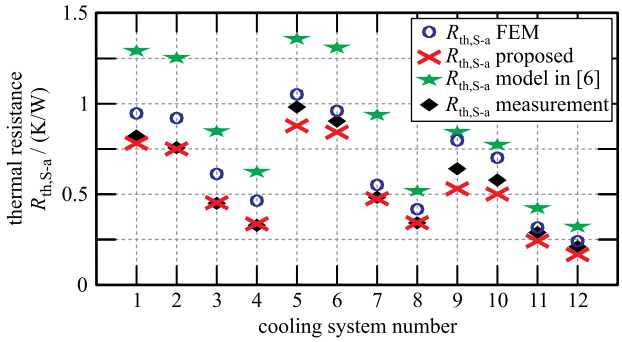


Fig. 14. Comparison of measurements (black diamonds) to the results obtained from FEM simulations (blue dots), the cooling system model given in [6] (green stars), and the proposed cooling system model (red crosses) [cf., Table III].

Fig. 14 summarizes the results obtained from measurements, FEM simulations, the proposed analytical model, and the model detailed in [6]. The mean deviations are 19.5% for FEM, 8% for the new model, and 58% for the model in [6].

## VI. Discussion

According to the results attained in Sections III and V the proposed model is considerably better suited for weight optimization than the previous model in [6], as it more accurately models the behavior of the fluid dynamic and thermal

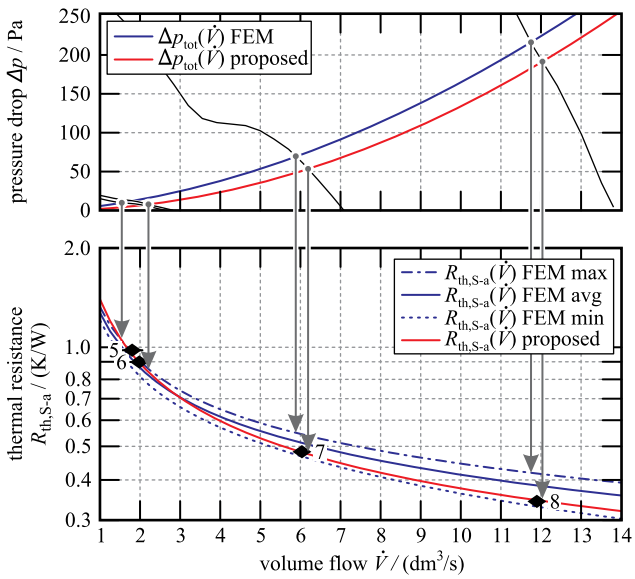


Fig. 15. Comparison of measured cooling systems 5–8, (black diamonds), cf., Table III, to the thermal and fluid dynamic characteristics $\Delta p_{\mathrm{tot}}(\dot{V})$ and $R_{\mathrm{th,S\text{-}a}}(\dot{V})$, attained with FEM simulation results and the proposed cooling system model.

characteristics $\Delta p_{\mathrm{tot}}(\dot{V})$ and $R_{\mathrm{th,S\text{-}a}}(\dot{V})$. The fluid dynamic model includes the most important phenomena, i.e., fluid friction at the walls, sudden contraction, sudden expansion, and conservation of momentum. The main improvements of the thermal model are as follows: the use of a single fluid heat exchanger model (4) (instead of a convective model [6]); the use of a fin efficiency model (5); and the use of the Nusselt number model (6), developed in [11].

The measurement results demonstrate a very good matching of calculated, FEM simulated, and measured results for the realized cooling systems. The great difference between the calculation of the thermal resistance $R_{\mathrm{th,S\text{-}a}}$, by means of FEM simulations and analytical modeling, lies in the computational time required to achieve an optimization result: the analytical model requires less than 20 s, on a personal computer, to evaluate 2000 geometries with the ten fans listed in Table I, whereas FEM simulations often require hours to determine the results for a single geometry. The accuracies of the thermal resistances $R_{\mathrm{th,S\text{-}a}}$ calculated with the proposed thermal model are found to be similar to the accuracies of the results obtained from thermal 3-D FEM simulations if both, thermal model and FEM simulation, are conducted for the same (predetermined) volume flow. With thermal 3-D FEM simulations, however, additional details may be obtained, e.g., hot spot temperatures on the heat sink's interface surface.[2]

Fig. 15 shows the pressure drop and thermal characteristics $\Delta p_{\mathrm{tot}}(\dot{V})$ and $R_{\mathrm{th,S\text{-}a}}(\dot{V})$ of the measured cooling systems 5–8, cf., Table III, obtained by 3-D FEM simulation and the analytical model. As FEM simulation results provide a temperature distribution instead of thermal resistances, the maximum, mean, and minimal temperatures on the heat sink's interface surface are translated into equivalent thermal resistances. For the cooling systems 5 and 6, the FEM simulated and the calculated thermal resistance characteristics $R_{\mathrm{th,S\text{-}a}}(\dot{V})$ (the blue and the red curves in Fig. 15) are almost identical. The differences between the FEM simulated and the calculated thermal resistance values for the cooling systems 5 and 6, as shown in Fig. 14, can be explained by differences in simulated and calculated pressure drops $\Delta p_{\mathrm{tot}}(\dot{V})$, which lead to different volume flows and thermal resistances. The thermal resistances $R_{\mathrm{th,S\text{-}a}}(\dot{V})$ of the cooling systems employing the fans MC19660 and GM0504PEV2-8.GN, i.e., {1, 2, 5, 6, 9, 10}, are found to be particularly sensitive to minor errors in the estimations of $\Delta p_{\mathrm{tot}}(\dot{V})$. For these systems, a change in the fan speed of $\pm 10\%$, which is achieved by changing the supply voltage by $\pm 10\%$, considerably changes the resulting thermal resistance. The thermal resistance measured for cooling system number 6, for example, would match the FEM simulation result if the rotational speed of the corresponding fan, i.e., MC19660, is 10% lower; if this fan rotates 10% faster, the measurement would match the calculated result.[3]

Fig. 15 shows that the calculation of the volume flow is less sensitive on an error of the calculated or simulated pressure drop for cooling system 7, since, at the intersection point, the slope of the characteristic of the corresponding fan, i.e., $d[\Delta p_{\mathrm{fan}}(\dot{V})]/d\dot{V}$, is greater than for the fans of cooling systems 5 and 6. The same holds for cooling system 8. This can be explained based on the fan affinity laws, since, for a given fan diameter (which is the same for all fans considered in this work), the volume flow increases linearly with the revolution speed and the pressure drop increases quadratically with the revolution speed [20].

According to the results obtained from 3-D FEM simulations, the cooling systems 7 and 8 (volume flows between $\dot{V} = [5, 12]$ dm$^3$/s) and for $P_{\mathrm{loss}} = 80$ W, the differences between the base plate temperatures near the outlet ($T_{\mathrm{hs,max}}$) and near the inlet ($T_{\mathrm{hs,min}}$) are in the range $T_{\mathrm{hs,max}} - T_{\mathrm{hs,min}} = [6.3, 6.8]$°C. The corresponding maximum temperature rises of the heat sink, i.e., $T_{\mathrm{hs,max}} - T_{\mathrm{amb}} = [47.2, 33.1]$°C, decrease by approximately 21% if the volume flow increases from 5 dm$^3$/s to 12 dm$^3$/s. Thus, for heat sinks with comparably low thermal resistance $R_{\mathrm{th,S\text{-}a}}$ achieved by means of a high volume flow, heat spreading effects may have a considerable impact on the total thermal resistance and need to be considered, e.g., according to [19]. Including the effect of heat spreading, i.e., $R_{\mathrm{th},d}$ is replaced with the expressions in [19], yields a change in the total thermal resistance $R_{\mathrm{th,S\text{-}a}}$ from 0.98 to 1.02 K/W (cooling system 5) and from 0.341 to 0.368 K/W (cooling system 8). At $P_{\mathrm{loss}} = 80$ W, this is a temperature difference of $T_{\mathrm{hs,max}} - T_{\mathrm{hs,min}} = 3.5$°C for both realized cooling systems 5 and 8.

In a final step, the cooling systems attained with the proposed optimization procedure (see Fig. 11) and the optimization procedure presented in [7] are compared with respect to the total weights, by applying the procedure to the case study provided in [7]. Using the fan MC25060V1 in combination with a ducted heat sink featuring the dimensions $b = 25$ mm, $d = 4$ mm,

[2]If required, the proposed thermal model can be extended with respect to heat spreading effects, e.g., using the approach presented in [19].

[3]For the underlying calculations, the fan characteristic has been scaled according to the fan affinity laws [20].

$c = 12$ mm, $n = 8$, $t = 1$ mm, and $L = 20$ mm, only 19.1 g is required to achieve a thermal resistance of 2.5 K/W, whereas the cooling system in [7] requires 31.3 g, i.e., 64% more weight.

## VII. Conclusion

This paper has presented a weight optimization procedure for forced convection cooling systems that are composed of an extruded-fin heat sink and a fan. It details the optimization of the number of air channels employed and the heat sink's fin thickness and length, with respect to minimum weight. Furthermore, the selection of a suitable fan, which yields minimum total weight of the cooling system, is presented. An analytical cooling system model is detailed and compared to the results obtained from FEM simulations and from an existing cooling system model detailed in [6].

The presented experimental results document the effectiveness of the proposed cooling system model and optimization procedure. A comparison of a selected experimental cooling system with $R_{\mathrm{th,S\text{-}a}} = 0.98$ K/W and $m_{cs} = 75$ g to commercially available products, of equivalent thermal resistance $R_{\mathrm{th,S\text{-}a}} \approx 1$ K/W, e.g., miniature cooling aggregate LAM 4, manufactured by Fischer Elektronik, with heat sink dimensions of $40$ mm $\times$ $40$ mm $\times$ $60$ mm and total weight $m_{\mathrm{cs}} = 157$ g, reveals a weight reduction of 52%.

## References


[1] J. W. Kolar *et al.*, "Conceptualization and multi-objective optimization of the electric system of an airborne wind turbine," in *Proc. 20th IEEE ISIE*, Gdansk, Poland, Jun. 27–30, 2011, pp. 32–55.

[2] R. A. Friedemann, F. Krismer, and J. W. Kolar, "Design of a minimum weight dual active bridge converter for an airborne wind turbine system," in *Proc. 27th APEC*, Orlando, FL, USA, Feb. 5–9, 2012, pp. 509–516.

[3] M. B. Dogruoz and M. Arik, "On the conduction and convection heat transfer from lightweight advanced heat sinks," *IEEE Trans. Compon. Packag. Technol.*, vol. 33, no. 2, pp. 424–431, Jun. 2010.

[4] S. Lee, "Optimum design and selection of heat sinks," *IEEE Trans. Compon., Packag. Manuf. Technol. A*, vol. 18, no. 4, pp. 812–817, Dec. 1995.

[5] M. F. Holahan, "Fins, fans, form: Volumetric limits to air-side heatsink performance," *IEEE Trans. Compon. Packag. Technol.*, vol. 28, no. 2, pp. 255–262, Jun. 2005.

[6] U. Drofenik, A. Stupar, and J. W. Kolar, "Analysis of theoretical limits of forced-air cooling using advanced composite materials with high thermal conductivities," *IEEE Trans. Compon., Packag. Manuf. Technol.*, vol. 1, no. 4, pp. 528–535, Apr. 2011.

[7] P. Ning, F. Wang, and K. D. T. Ngo, "Forced-air cooling system design under weight constraint for high-temperature SiC converter," *IEEE Trans. Power Electron.*, vol. 29, no. 4, pp. 1998–2006, Apr. 2014.

[8] R. J. Moffat, "Modeling air-cooled heat sinks as heat exchangers," in *Proc. 23rd Annu. IEEE SEMI-THERM*, San Jose, CA, USA, Mar. 18–22, 2007, pp. 200–207.

[9] Y. S. Muzychka, "Generalized models for laminar developing flows in heat sinks and heat exchangers," *Heat Transfer Eng.*, vol. 34, no. 2/3, pp. 178–191, 2013.

[10] P. Teertstra, M. M. Yovanovich, J. R. Culham, and T. Lemczyk, "Analytical forced convection modeling of plate fin heat sinks," in *Proc. 15th Annu. IEEE Semicond. Thermal Meas. Manag. Symp.*, Mar. 1999, pp. 34–41.

[11] Y. S. Muzychka and M. M. Yovanovich, "Laminar forced convection heat transfer in the combined entry region of non-circular ducts," *ASME Trans.*, vol. 126, no. 1, pp. 54–61, Feb. 2004.

[12] F. M. White, *Fluid Mechanics,* 4th ed. New York, NY, USA: McGraw-Hill, ser. Mechanical Engineering.

[13] Y. Shabany, *Heat Transfer: Thermal Management of Electronics*. New York, NY, USA: Taylor & Francis, 2009, pp. 281–283.

[14] J. R. Culham, W. A. Khan, M. M. Yovanovich, and Y. S. Muzychka, "The influence of material properties and spreading resistance in the thermal design of plate fin heat sinks," *J. Electron. Packag.*, vol. 129, no. 1, pp. 76–81, 2007.

[15] Y. S. Muzychka and M. M. Yovanovich, "Pressure drop in laminar developing flow in noncircular ducts: A scaling and modeling approach," *J. Fluids Eng.*, vol. 131, no. 11, p. 111105, Nov. 2009.

[16] W. Kays, M. Crawford, and B. Weigand, *Convective Heat and Mass Transfer*. New York, NY, USA: McGraw-Hill, 1977.

[17] V. D. Ingenieure, *VDI-Wärmeatlas,* 10th ed. Berlin, Germany: Springer-Verlag, 2006, p. 945, (in German).

[18] ASHRAE Research, *Fundamentals: 2005 Ashrae Handbook: Si Edition*, Amer. Soc. Heating, Atlanta, GA, USA, 2005.

[19] S. Song, V. Au, S. Lee, and K. P. Moran, "Constriction/spreading resistance model for electronics packaging," in *Proc. 4th ASME/JSME Thermal Eng. Joint Conf.*, 1995, vol. 4, pp. 199–206.

[20] S. L. Dixon, *Fluid Mechanics and Thermodynamics of Turbomachinery,* 4th ed. Oxford, U.K.: Butterworth-Heinemann, 1998.


**Christoph Gammeter** (S'13) received the M.Sc. degree from the Swiss Federal Institute of Technology (ETH) Zürich, Zürich, Switzerland, in 2012. He is currently working toward the Ph.D. degree in the Power Electronic Systems Laboratory (PES), ETH Zürich, where he is working on weight-optimized converters.

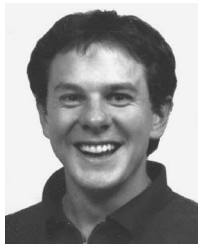

**Florian Krismer** (S'05–M'12) received the M.Sc. degree from the University of Technology Vienna, Vienna, Austria, in 2004 and the Ph.D. degree from the Power Electronic Systems Laboratory (PES), Swiss Federal Institute of Technology (ETH) Zürich, Zürich, Switzerland, in 2011.

He is currently a Postdoctoral Fellow with PES, ETH Zürich. His research interests include the analysis, design, and optimization of high-current and high-frequency power converters.

**Johann W. Kolar** (F'10) received the M.Sc. degree and the Ph.D. degree (*summa cum laude*) from the University of Technology Vienna, Vienna, Austria.

He is currently a Full Professor with the Swiss Federal Institute of Technology (ETH) Zürich, Zürich, Switzerland, where he is also the Head of the Power Electronic Systems Laboratory. He has proposed numerous novel pulsewidth-modulation converter topologies, and modulation and control concepts, e.g., the Vienna rectifier, the Swiss rectifier, and the three-phase ac–ac sparse matrix converter, and he has published over 600 scientific papers in international journals and conference proceedings and has filed more than 100 patents. His current research interests include ultracompact and ultraefficient converter topologies employing latest power semiconductor technology (SiC and GaN), solid-state transformers, power supplies on chip, and ultrahigh-speed and bearingless motors.

Dr. Kolar was a recipient of nine IEEE Transactions Prize Paper Awards, eight IEEE Conference Prize Paper Awards, the SEMIKRON Innovation Award 2014, and the ETH Zürich Golden Owl Award 2011 for Excellence in Teaching.